Wall Heat Flux Evaluation in Regeneratively Cooled Rocket Thrust Chambers

Nikolaos Perakis,* Lukas Preis,† and Oskar J. Haidn‡
Technical University of Munich, 85748 Garching, Germany

https://doi.org/10.2514/1.T6056

In the present Paper, different wall heat flux evaluation methods for rocket engines are analyzed and compared. The test case for the comparison is a supercritical load point of an H_2/O_2 upper-stage engine. The evaluation of the heat flux using existing gradient methods shows unacceptable deviations, whereas significant improvements are found with an inverse heat transfer method. Using a Nusselt number correlation for the modeling of the cooling channel heat transfer coefficient, good agreement with the experimental profiles is achieved, while the number of installed thermocouples is held at a minimum. However, the choice of the Nusselt number correlation directly influences the obtained results and strongly depends on the fuel and geometry of the system. Using a simultaneous optimization of the heat flux and heat transfer coefficient, on the other hand, seems to eliminate the need for additional modeling and leads to great agreement with the experiment. A new optimization method proposed in this Paper based on a preprocessed Jacobi matrix significantly speeds up the estimation of the free parameters. With the obtained results, the placement of the thermocouples before the design of the hardware can be optimized, leading to reduction of manufacturing costs.

Nomenclature

A	=	area, m^2
AR	=	aspect ratio
c^*	=	characteristic velocity, m/s
c_p	=	specific heat capacity, $J/(kg \cdot K)$
D	=	diameter, m
d	=	absolute thermocouple distance, m
H	=	specific enthalpy, J/kg
$\boldsymbol{H}$	=	heat transfer coefficient parameters, $W/(m^2 \cdot K)$
h	=	heat transfer coefficient, $W/(m^2 \cdot K)$
I_{sp}	=	specific impulse, s
J	=	residual/objective function, K^2
M	=	number of thermocouples
$\dot{m}$	=	mass flow rate, s
N	=	number of optimization parameters
Nu	=	Nusselt number
$\boldsymbol{n}$	=	wall normal, m
O/F	=	oxidizer to fuel ratio
p	=	pressure, bar
Pr	=	Prandtl number
$\boldsymbol{Q}$	=	wall heat flux parameters, W/m^2
$\dot{q}$	=	wall heat flux, W/m^2
Re	=	Reynolds number
r	=	radial distance, m
$\boldsymbol{S}$	=	sensitivity matrix, $(K \cdot m^2)/W$
T	=	temperature, K
t	=	wall thickness, m
x	=	axial distance, m
y	=	wall distance, m
z	=	spanwise distance, m
δ	=	relative thermocouple distance, m
λ	=	thermal conductivity, $W/(m \cdot K)$

Subscripts

bottom	=	bottom wall
c	=	calculated
cc	=	cooling channel
ch	=	combustion chamber
dev	=	standard deviation
err	=	error
f	=	fluid (coolant)
h	=	hydraulic
hgw	=	hot gas wall
in	=	inlet
m	=	measured
n	=	normalized
out	=	outlet
$side$	=	side wall
t	=	turbulent
top	=	top wall
w	=	wall

I. Introduction

THE high velocity flows within liquid propellant rocket engines combined with the hot gas temperatures of around 3500 K give rise to extreme heat loads at the wall of a typical rocket thrust chamber. When designing a rocket engine, a high chamber pressure is typically beneficial, as it helps achieve a high specific impulse and increases the compactness of the chamber [1]. A higher combustion chamber pressure, however, has a direct impact on the wall heat loads, because the heat transfer coefficient is proportional to the chamber pressure ($\dot{q} \sim p^{0.8}$) [2].

To ensure the reliable operation of rocket thrust chambers at those high operating thermal loads, efficient cooling methods need to be implemented such as film cooling, regenerative cooling, or a combination of the two. The proper design of the cooling system requires sufficient understanding of the heat transfer methods within the chamber and the wall structure not only to minimize the plastic deformation and ensure the desired component life but also because in some engine cycles the performance relies on the heat transfer characteristics between the hot gas and the wall. A typical example is the expander cycle, where the turbopumps are driven by the enthalpy that the cooling fluid picks up while flowing through the channels along the chamber wall.

To design a rocket engine, numerical methods are often implemented in order to simulate the flow structures within the thrust

Received 7 April 2020; revision received 20 May 2020; accepted for publication 9 July 2020; published online 30 September 2020.

*Graduate Student, Chair of Space Propulsion, Boltzmannstrasse 15; nikolaos.perakis@ltf.mw.tum.de.

†Graduate Student, Chair of Space Propulsion, Boltzmannstrasse 15.

‡Professor, Chair of Space Propulsion, Boltzmannstrasse 15.

chamber. These computational fluid dynamics (CFD) simulations are important in the first stages of an engine design because they can replace expensive trial-and-error firing tests. Nevertheless, for those models and simulations to be considered reliable, sufficient validation is mandatory. This is usually done by comparing their predicted heat flux, pressure, and performance (c^*, I_{sp}) against predefined experimental test cases [3,4]. For this validation, it is hence essential that the provided heat flux measurements are reliable and that sources of potential systematic errors are known.

It is therefore evident that the ability to accurately determine the heat loads of a rocket engine are very important for the design of future hardware, for the evaluation of hot-gas experiments and the validation of CFD models. Heat flux measurements can, however, be quite challenging. Although pressure, mass flow rate, thrust, and combustion efficiency are not challenging to measure during a hot run test, information on the temperature and heat loads at the chamber walls can be difficult to obtain due to the harsh environment. To improve the heat flux prediction accuracy in rocket combustors, significant efforts have been put into designing experimental research combustors, allowing for precise heat transfer measurements [5–9].

The purpose of the present Paper is to present the benefits of using inverse heat transfer methods for estimating the locally varying heat loads in regeneratively cooled rocket engines. Using a baseline reference case of a full-scale upper-stage engine described in Sec. III, a comparison between the different heat flux evaluation methods is presented. The main focus and innovation of this Paper lie in identifying the influence of the thermocouple placement on the achieved accuracy of each method shown in Sec. IV. Based on the available number of installed thermocouple sensors, the most accurate evaluation method is assessed. We are able to show that even a single thermocouple for each axial position is sufficient for an accurate heat flux retrieval. For a computationally efficient evaluation of the three-dimensional problem with arbitrary number of sensors, an optimization algorithm is presented in Secs. IV.B and IV.C. Although the idea of simultaneous optimization of wall heat flux and coolant heat transfer coefficient shown in these sections is not new, the proposed algorithm for the inversion significantly reduces the computational resources needed compared to methods used in the past.

II. Heat Flux Measurement Methods

In most rocket engines, the heat flux distribution has a three-dimensional nature with variations along the azimuthal direction (especially close to the face plate due to thermal and species stratification) and along the axial direction due to the progress in chemical reaction and the acceleration in the nozzle. Therefore, heat transfer measurements, apart from performing accurate estimations of the maximal heat loads, are required to resolve the spatial distribution of the thermal fields in order to deliver information about the mixing and reactions in the chamber.

Measurement specimens such as thermal barrier coatings have been developed in order to carry out a direct heat flux measurement; however, they are usually prone to large measurement uncertainty [10]. Heat flux sensors such as the Gardon sensor [11], the anisotropic heat flux sensors, and high-temperature heat flux sensors [12] were also developed for heat measurements but for other engineering applications. Although they can provide acceptable local resolution, their disadvantages include a difficult integration, disturbance of the temperature field due to the hot-island effect, a limited maximal operating temperature, and low maximal heat flux. Because of their lacking reliability when dealing with high thermal loads, they are rarely implemented in rocket engines. Instead, the most common methods for measuring heat fluxes are the calorimetric method, the transient method, the gradient method, and the inverse method. Most transient methods are applied in capacitively cooled chambers and are hence not relevant in the case of actively cooled thrusters. More information can be found in the work by Celano et al. [13].

A. Calorimetric Method

The presence of an active regenerative cooling system in most rocket engines experiencing high thermal loads allows for the application of the calorimetric method to determine the wall heat loads. Specifically, if the structure being cooled by a cooling fluid is in thermal equilibrium (no transient phenomena) and the natural convection of the outer walls is neglected, then the heat flow rate into the structure is equal to the heat flow rate from the material into the cooling fluid. The total heat rate coming from the hot-gas wall can therefore be determined by measuring the enthalpy increase of the coolant between the inlet and outlet of the channel. The average heat flux in the segment can then be calculated according to Eq. (1):

$$\dot{q} = \frac{\dot{m}_f}{A_w} \cdot [H_f(p,T)_{\text{out}} - H_f(p,T)_{\text{in}}] \tag{1}$$

The wall area A_w refers to the total area exposed to the hot gas within the segment. The method is very common, because it requires only the measurement of the coolant mass flow rate $\dot{m}_f$ and the pressure and temperature of the fluid at the inlet and outlet positions. Because the accuracy of those three individual measurements is within 1%, the errors in the average heat flux estimation using the calorimetric principle are limited. Note, that in order for the method to be effective the axial heat transfer between separate segments has to be negligible; otherwise, an additional source of error is introduced as seen in the work by Perakis et al. [14]. This can be achieved if the coolant of the first segment is used as well for the subsequent segments to minimize coolant temperature differences at the interface.

Therefore, global heat flux characteristics can be estimated with confidence using the calorimetric method. However, the resolution of this method is limited by the number of cooling segments present in the configuration. Most of the times, the method is connected to limited spatial resolution due to the additional complexity in the case of a large cooling segment number. When a more detailed resolution is required, other methods would have to be implemented, allowing for a more dense heat flux measurement distribution. A further disadvantage of the calorimetric method is the difficulty in determining the wall temperature from the heat flux measurement. Because only an average heat flux is estimated, the local profile of wall temperature is very challenging to calculate.

B. Gradient Method

The gradient method is a simplified procedure which allows for the estimation of local heat flux and wall temperature not only for actively cooled but also capacitively cooled chambers and relies on the measurement of temperature at several radial distances from the hot-gas wall (usually 2 to 5). By estimating the temperature gradient in the direction normal to the structure wall, the heat flux can be approximated. In the case of cylindrical chambers, the heat flux is given by

$$\dot{q}(r) = \frac{\lambda(T_2 - T_1)}{\ln(r_1/r_2) \cdot r_{\text{ch}}} \tag{2}$$

Calculating the heat flux requires at least two thermocouple measurements in different radial positions r_i. The benefit of the method is its very low computational complexity. Although the method is very accurate when dealing with capacitive cooling, the approximation that the heat flux follows the form given in Eq. (2) can become invalid when cooling channels are employed. The distortion of the temperature field by the cooling system leads to a more complex, nonanalytic expression for the wall heat flux, and the use of Eq. (2) can cause large systematic deviations.

C. Inverse Heat Transfer Method

A more reliable method for the evaluation of the wall heat transfer is based on the inverse solution of the thermal heat transfer problem. Inverse methods for heat transfer are typically iterative methods, which employ an optimization procedure to estimate the value of an

unknown boundary conditions that best matches the experimentally measured temperatures [15].

Inverse methods have been applied successfully in various engineering applications ranging from solar tower power plants [16], mold casting [17], internal combustion chambers [18], rocket combustion thrust chambers [4,19,20], sounding rockets [21], and induction heating [22]. Although all methods have in common that an optimization of the unknown boundary conditions is carried out, the exact methods for finding the optimal solution are quite diverse. Studies can be found in the literature including classical optimization based on adjoint methods [23], conjugate gradient methods [18], the Newton–Raphson method [4], the Levenberg–Marquardt algorithm [24,25], genetic algorithms [26,27], neural networks [17] as well as noniterative boundary element methods [28,29], and noniterative finite element methods [30]. In all of them, however, the objective is the minimization of the residual J,

$$J(\boldsymbol{Q}) = \frac{1}{M} \cdot [\boldsymbol{T}_m - \boldsymbol{T}_c(\boldsymbol{Q})]^T [\boldsymbol{T}_m - \boldsymbol{T}_c(\boldsymbol{Q})] \tag{3}$$

which describes the differences between the measured $\boldsymbol{T}_m$ and calculated $\boldsymbol{T}_c$ temperature vectors for a given choice of heat flux parameters $\boldsymbol{Q}$.

When dealing with experimental inverse methods, the available information consists of temperature measurements in M distinct positions within the material. For the problem to be well posed, the number of optimization variables N on the unknown boundary (the heat flux $\dot{q}$ in most applications) has to be smaller than or equal to the number of available measurement positions M [15]. Choosing the positioning of the thermocouples is hence very important when designing the experiment. In general, choosing thermocouple positions as close to the location of the optimization parameter as possible is beneficial in order to ensure the highest sensitivity and avoid parameter interference [31,32].

In the case of rocket thrust chambers used for main and upper stages of launch vehicles, a regenerative cooling system is typical [1]. On the one hand, the cooling system simplifies the inverse simulation as it eliminates the need for a transient solution, when the chamber operates in study state (excluding the startup and shutdown phases) as opposed to capacitively cooled chambers [20]. On the other hand, a further unknown boundary conditions is introduced to the system, namely, the heat transfer coefficient between the structure and the cooling channels h_{cc}.

The prediction of this additional unknown boundary simultaneously to the hot gas wall heat load can be performed with two different methods: modeling and optimizing.

1. *Modeling Cooling Channel Heat Transfer Coefficient*

In the first method, the interaction between the coolant and the structure is carried out either using a CFD simulation or with a simpler correlation (e.g., a Nusselt number correlation for h_{cc}). In the case of CFD, the sophistication and accuracy is expected to be higher than for simpler one-dimensional expressions. The higher accuracy is expected due to the threedimensional nature of the cooling channel simulation, which allows for the prediction of local variations of the heat transfer coefficient, both in axial and circumferential direction, while also capturing physical effects like thermal stratification [33] and heat flux deterioration [34,35]. Nevertheless, the computational time can be significantly higher, due to the iterative nature of the optimization algorithms, requiring multiple solutions of the CFD algorithm.

In the case of Nusselt number correlations, on the other hand, the computational resources needed are minimal. However, because of the simplified nature of the correlations which typically provide only a one-dimensional profile of h_{cc} along the channel axis, a higher uncertainty is expected, especially for supercritical conditions. Efforts are being carried out, however, to improve the correlations and increase their complexity by incorporating corrections for heat flux deterioration phenomena [36], supercritical conditions [37], and curvature effects [38]. Using new advances in neural networks can also assist in improving the existing correlations for hydrocarbon rocket engines [39].

Regardless of the chosen modeling option, a further benefit of this method is the reduction of the free optimization parameters. Because the calculation of the heat transfer coefficient is carried out with CFD or a correlation, the only remaining unknown parameter is the wall heat flux $\dot{q}$. For that reason, the use of only one thermocouple per position is sufficient to ensure well-posed-ness. This method uses the minimal amount of installed sensors and has been successfully applied in water-cooled rocket thrust chambers [4].

2. *Optimizing Cooling Channels Heat Transfer Coefficient*

The second option classifies the cooling channel heat transfer coefficient as an additional unknown, similar to the wall heat flux. The benefit of this method is that no additional modeling is required for the solution of the thermal problem. Because both the hot-gas wall boundary and the cooling channel wall boundary are modeled as black boxes, the domain only consists of the chamber material, and the only modeling parameters are the material properties like thermal conductivity, heat capacity, and density. The accumulated effect of thermal stratification, heat transfer deterioration, curvature, and wall roughness is captured without the need of additional models.

Nevertheless, because of the increased number in free optimization parameters, the demand for more thermocouple measurements is also higher, resulting in $M \geq 2 \cdot N$. Because of the larger number of free parameters, the simultaneous optimization of $\dot{q}$ and h_{cc} can become computationally intensive. In Sec. IV.C, a computationally efficient method based on the sensitivity matrix is introduced.

III. Test Case Description

To demonstrate the performance of each heat transfer evaluation method, a representative test case has been defined. Heat flux measurement methods are used both in subscale experimental chambers as well as in full-scale hardware being tested for qualification and acceptance. To ensure that the results of the current analysis are representative for flight hardware applications, a full-scale expander engine is used, operated with Liquid oxygen/liquid hydrogen.

The chosen hardware corresponds to the virtual thrust chamber demonstrator (TCD) presented in the work of Eiringhaus et al. [40]. The full-scale demonstrator TCD1 has been defined and designed with the purpose of testing the available numerical and analytical methods of combustion and heat transfer modeling [41].

The TCD1 concept is an upper-stage engine operating with an expander cycle and producing a nominal thrust of 100 kN, similar to the RL-10C engine [42]. The combination of LOX and LH_2 for the oxidizer and fuel are chosen as propellants. A nominal combustion chamber pressure of 55 bar and an o/F equal to 5.6 are chosen as a reference operating point. The nozzle extension has been designed according to the truncated ideal contour (TIC) principle. For the cooling of the combustion chamber as well as the nozzle extension (up to an expansion ratio of 22), liquid hydrogen flows through a cooling channel in a coflow configuration. In total, 138 cooling channels are present, equally distributed along the perimeter. The chamber and the liner are manufactured using oxygen-free copper due to its high conductivity, whereas the outer structural jacket consists of nickel. Despite the TCD1 being a virtual engine, not intended to be built and tested, its design underwent all engineering steps found at the development process of a real engine, and it therefore constitutes a realistic example for the implementation of the inverse heat transfer method.

For an estimation of each heat transfer evaluation method's accuracy, the knowledge of the real wall heat flux, coolant heat transfer rate, and wall temperature has to be known for the entirety of the domain. In experimental configurations, this can never be achieved, and hence a virtual experimental test case is set up. The process for the generation of the experimental data is illustrated in Fig. 1.

To obtain a realistic wall heat flux profile for the chosen load point, a CFD simulation of the flow and turbulent combustion within the chamber is carried out. The models used are briefly described in Sec. III.A. Using the obtained experimental wall heat load, a simulation of the chamber structure with the cooling channels is carried out as outlined in III.B. This delivers a representative temperature

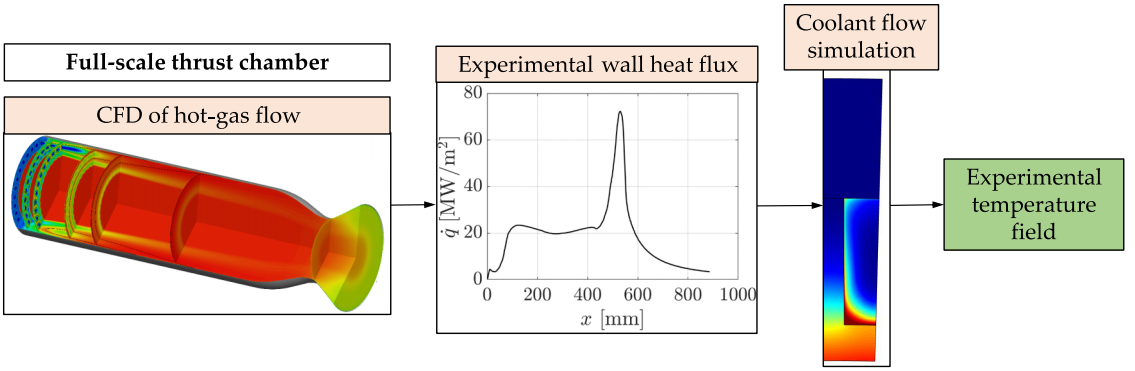

Fig. 1 Schematic illustration of the method used to generate the experimental test data.

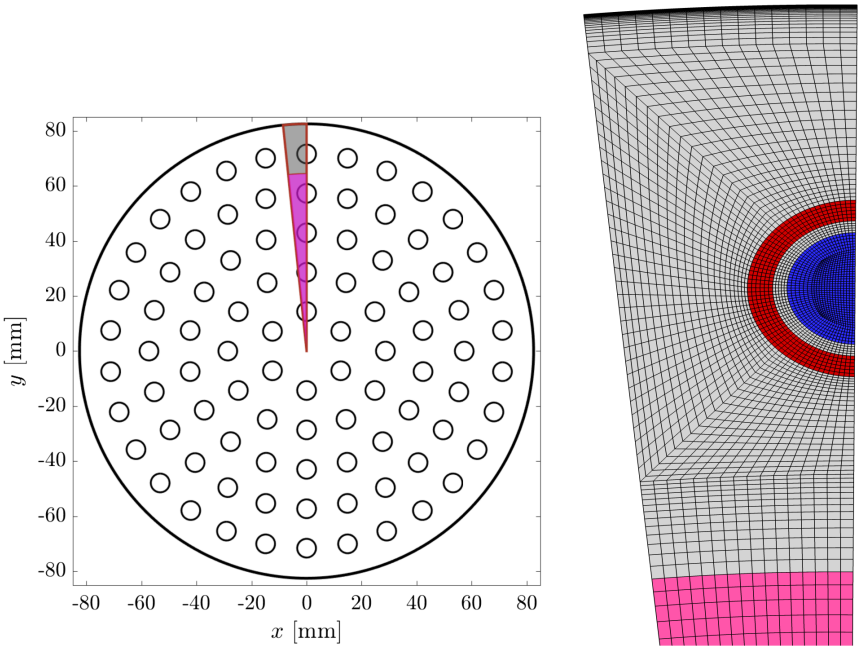

Fig. 2 Computational domain and mesh on the face plate. Note that every second grid point is shown.

field within the entire structure, which is used to generate the virtual thermocouple measurements.

A. Simulation of Hot-Gas Flow

A three-dimensional Reynolds-averaged Navier–Stokes (RANS) simulation of the supercritical combustion case within the TCD engine is carried out. The commercial code ANSYS Fluent has been used for the simulations [43]. To reduce the computational effort for the simulation of the hot-gas flow in the domain, only a thin sector of the engine is computed. In fact, the smallest possible symmetry is used, consisting of only half an injector in the outer row. The face plate as well as the chosen sector are illustrated in Fig. 4. To ensure that the symmetry of the injector configuration is attained, only the outermost injector is resolved, whereas the remaining mass flow rate is injected in premixed and preburnt conditions. The injection area of the preburnt mixture is indicated with the magenta color in Fig. 2. The red and blue colors represent the fuel and oxidizer inlet, respectively. This method of reducing the number of resolved injectors has been used in the past for simulations of full-scale engines [44,45] as it significantly reduces the computational cost while still preserving the three-dimensional nature of the flowfield and the injector/wall interaction. The resulting mesh consists of $2.3 \cdot 10^6$ cells, and its wall resolution is chosen so as to fulfill the $y^+ < 1$ condition. At the wall boundary, an axially varying temperature profile is applied, obtained from the work of Eiringhaus et al. [40].

Because of the fast chemical processes occurring in hydrogen/oxygen engines, a chemical equilibrium model has been employed for the turbulent combustion simulation. To account for the cryogenic injection temperatures of the liquid oxygen ($T_{ox} = 95$ K), a Peng–Robinson cubic equation of state is used [46], with the volume correction by Abudour et al. [47]. For the turbulence closure, the standard $k-\varepsilon$ model proposed by Launder and Spalding [48] is implemented, extended by the two-layer approach by Wolfshtein [49] to account for the proper treatment of the wall. A presumed

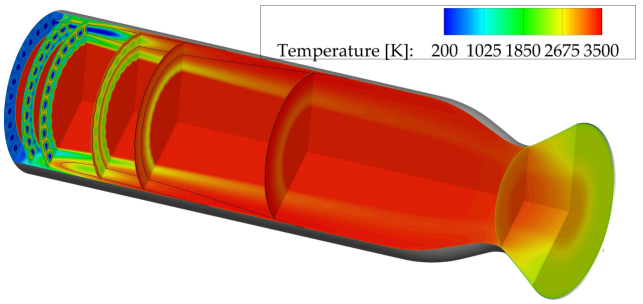

Fig. 3 Temperature field in the thrust chamber domain. The solid lines represent the stoichiometric composition.

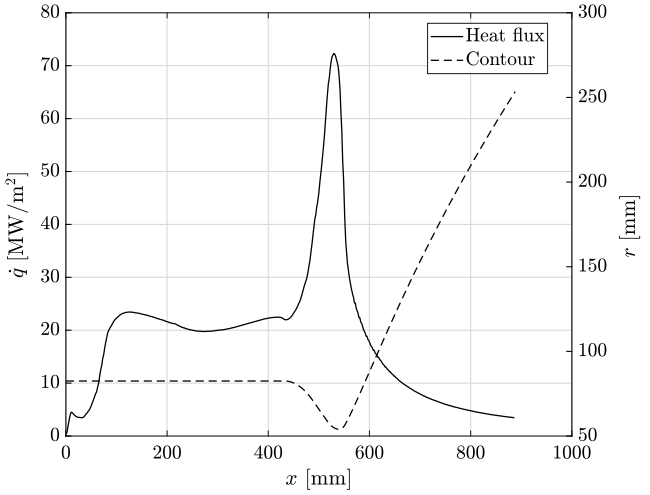

Fig. 4 Heat flux profile and chamber contour along the axial direction.

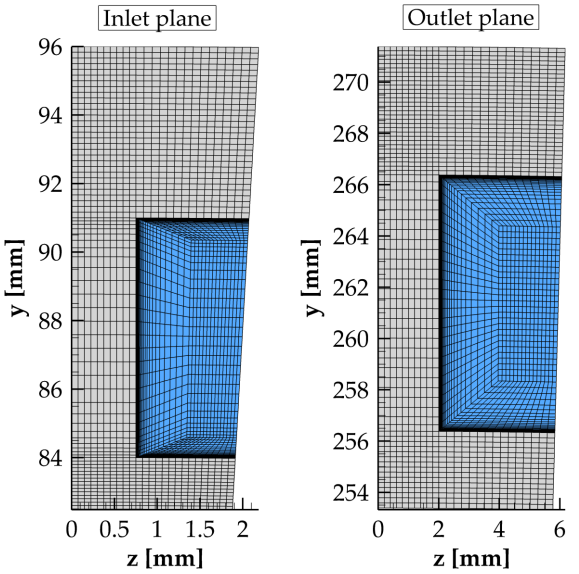

Fig. 6 Mesh at the inlet and outlet planes of the cooling channel.

β Probability Density Function is used for the turbulence/chemistry interaction, whereas constant turbulent Prandtl and Schmidt numbers equal to 0.9 and 0.6, respectively, are defined for the turbulent heat and mass fluxes. Finally, the molecular kinetic properties are defined using the model by Chung et al. [50], and for the thermodynamic data, NASA polynomials are used.

The resulting temperature distribution in the thrust chamber (excluding the nozzle extension) is shown in Fig. 3, in which the domain has been mirrored in the circumferential direction. The fact that the outer injector row is resolved gives rise to a temperature stratification close to the chamber wall. A liquid oxygen core can be identified, surrounded by a thin flame. The core flow, however, is injected in a preburnt state and hence remains uniform for the entire length of the domain. Because of mixing within the chamber, the gas composition and temperature become more homogeneous further downstream of the face plate. The resulting (circumferentially averaged) heat flux profile along with the chamber contour is plotted in Fig. 4. As expected, a rise in heat flux occurs within the first 100 mm from the injection plane, as the mixing and energy release within the outer injector is intensified. Farther downstream, the heat flux obtains a nearly constant value before increasing again in the converging part of the nozzle.

It is important to note here that the obtained heat flux values and combustion simulation results are not evaluated with regard to their validity and accuracy. Instead, they serve as realistic reference values, used for the generation of the experimental temperatures in Sec. B.

B. Numerical Setup of the Coolant Side

To calculate the material temperatures for the virtual reference experiment, a simulation of the hydrogen cooling channels and the chamber domain is carried out. To take advantage of the geometry's symmetry, only half of the 138 channels is included in the computational domain, leading to a simulation of only 1.3 deg. The domain with labels indicating the individual parts is illustrated in Fig. 5. A symmetry boundary condition is used for the other half of the cooling channel, which leads to $1.4 \cdot 10^6$ cells in the domain. A closeup of the mesh in the inlet and outlet planes is given in Fig. 6, in which the blue region indicates the fluid domain.

The hydrogen flow in the channel is modeled by solving the RANS equations. The $k-\omega$ shear-stress transport model by Menter [51] is chosen, and the wall is resolved to values of the dimensionless wall distance $y+$ of around 1. In all calculations, the closure of the turbulence flux terms is done with a constant turbulent Prandtl number $Pr_t = 0.9$. For the temperature-dependent properties of supercritical hydrogen, data from the National Institute of Standards and Technology library [52] have been used, accounting for pressure and temperature-dependent density, specific heat, viscosity, and thermal conductivity.

At the LH_2 inlet, the mass flow rate and the inlet temperature are given, whereas at the outlet, the expected pressure of 175 bar is set. The hot gas wall is given a von Neumann boundary condition with the applied heat flux from Fig. 1. Finally, the external jacket wall is defined as adiabatic. For the copper and nickel, temperature-dependent values for the density, heat capacity, and thermal conductivity are used. Only the energy equation is solved in the chamber material, and hence no significant modeling is required for the structure.

The temperature field within the chamber wall and hydrogen coolant is plotted in Fig. 7 for four locations within the chamber ($x = 100, 200, 300, 400$ mm) and the nozzle throat ($x = 541$ mm). As expected, due to the asymmetrical heating, the material and fluid

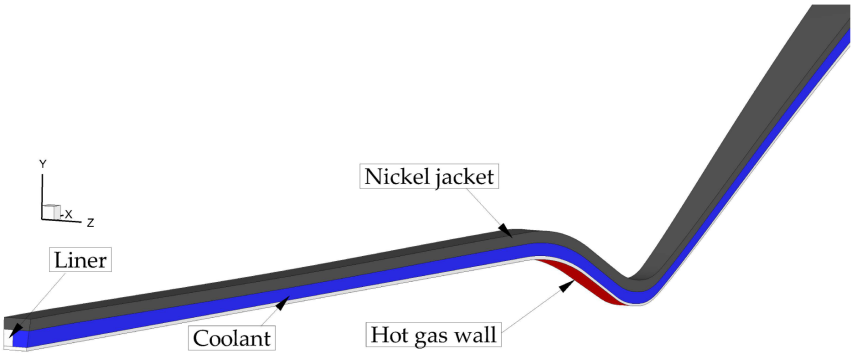

Fig. 5 Setup of the cooling channel simulation domain.

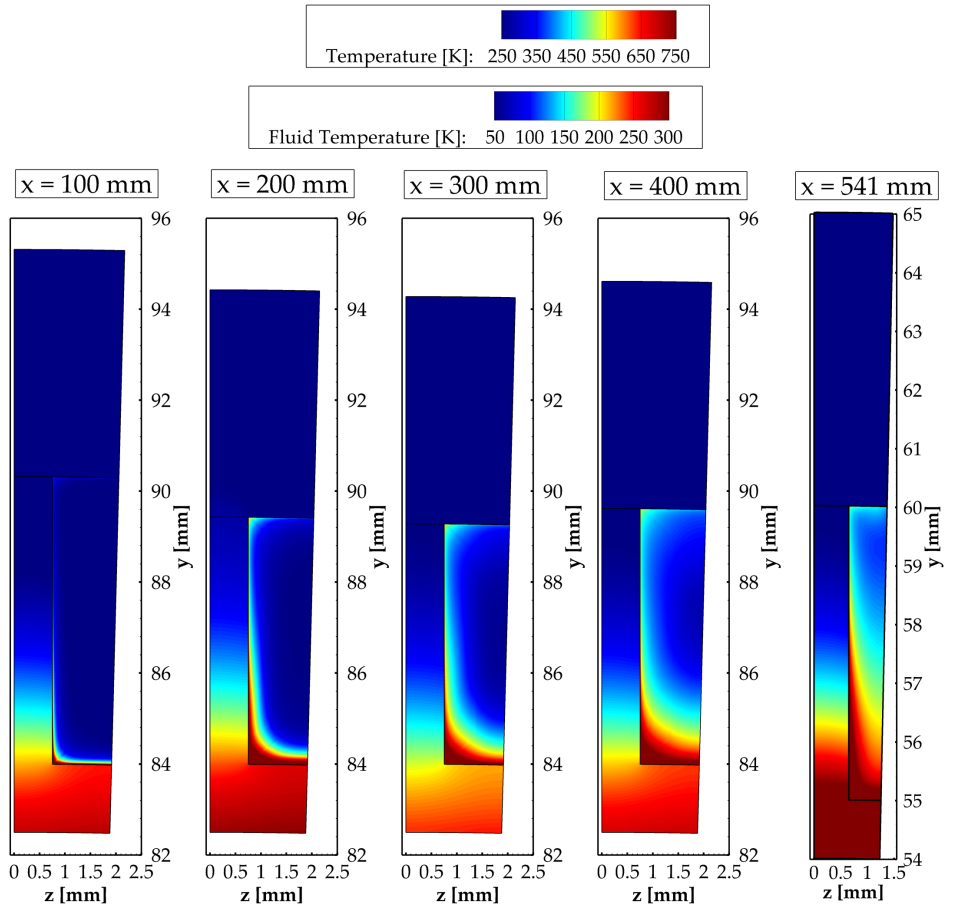

Fig. 7 Temperature field in the cooling channel for different axial positions.

temperatures close to the hot-gas wall are higher than the remaining locations. Moreover, because of the high thermal conductivity of the copper liner, a significant part of the heat is transferred radially outward, heating up the fluid in contact with the fins. This effects leads to an amplification of the thermal boundary layer dimensions along the bottom and vertical walls. This asymmetric heat attenuation leads to large deviations of the local temperature from the bulk flow temperature, i.e., to thermal stratification.

To describe the stratification more quantitatively, the standard deviation of the fluid temperature for each axial position $T_{f,\mathrm{dev}}$ is defined as the mass flow averaged discrepancy from the mean fluid temperature $T_{f,\mathrm{mean}}$:

$$T_{f,\mathrm{mean}} = \frac{\oiint_S T_f \, d\dot{m}}{\dot{m}} \tag{4}$$

$$T_{f,\mathrm{dev}} = \sqrt{\frac{\oiint_S (T_f - T_{f,\mathrm{mean}})^2 \, d\dot{m}}{\dot{m}}} \tag{5}$$

The axial profiles of both the mean temperature and the deviation are plotted in Fig. 8. For the bulk fluid temperature, a constant increase along the axial direction is observed. The temperature deviation, on the other hand, demonstrates a more complex profile. Specifically, it appears to be steadily increasing within the cylindrical part of the chamber and up to the throat (first 540 mm from the face plate). When entering the divergent part of the nozzle, a sudden drop in the standard deviation of the temperature occurs, indicating a more homogeneous fluid. The physical processes behind this phenomenon are not the subject to the present analysis but have been investigated in the past and are attributed to the secondary flows which change direction depending on the curvature of the channels [53]. The correlation between the performance of the inverse method and the temperature stratification will be discussed in Sec. IV.B.

Finally, the stratification of the temperature field gives rise in locally varying heat transfer coefficients along the channel circumference. In this context, the local heat transfer coefficient h is defined using the local wall temperature T_w and local channel heat flux $\dot{q}_w$:

$$h_{\mathrm{cc}} = \frac{\dot{q}_w}{T_w - T_{f,\mathrm{mean}}} \tag{6}$$

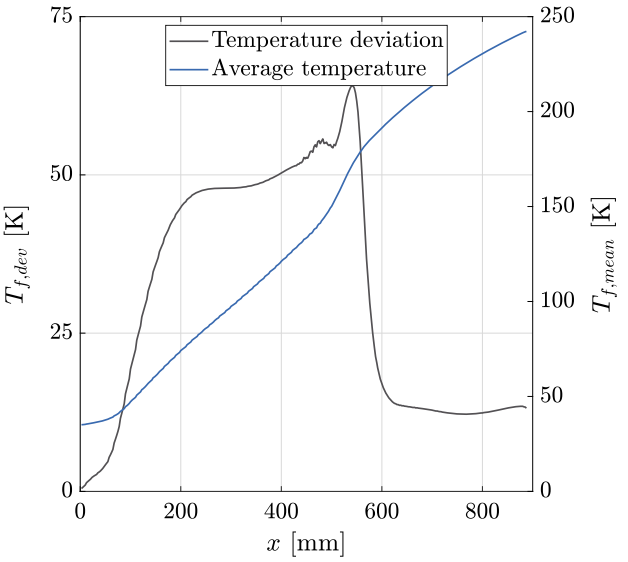

Fig. 8 Average coolant temperature and temperature stratification in the cooling channels.

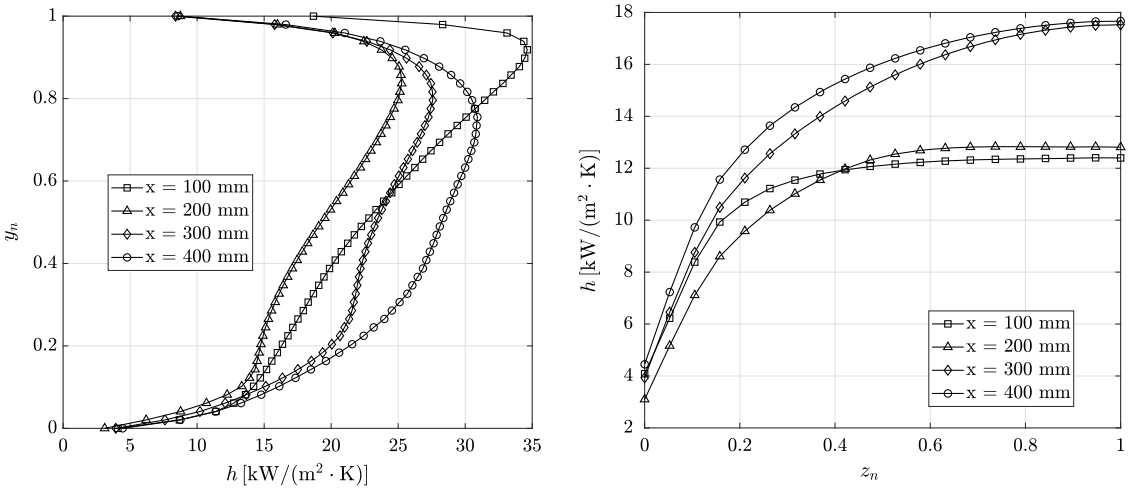

Fig. 9 Heat transfer coefficient for different axial positions along the vertical wall (left) and the horizontal bottom wall (right).

The variation along the normalized channel height y_n and the normalized channel width z_n is shown in Fig. 9. Note that $z_n = 1$ corresponds to the middle of the channel, $y_n = 0$ corresponds to the bottom wall, and $y_n = 1$ corresponds to the bottom wall. Given the observed variations of heat transfer coefficient along the channel circumference, the performance of the inverse heat transfer methods which approximate h_{cc} with a constant value for each axial position will be discussed in Sec. IV.D.

IV. Comparison of Heat Flux Evaluation Methods

Having established the test case used to generate the thermocouple measurements, we proceed with the analysis of the individual methods that were introduced in Sec. II. It is important to note that in this section only steady-state results are presented. The extension of the presented inverse methods to time-varying heat loads could also be carried out similar to the work by Perakis and Haidn [20].

Although the presented methods can be applied similarly to both the combustion chamber and the nozzle, the results within the chamber will be given more detailed focus. The reason is that the main mixing and combustion processes occur in the cylindrical part of the chamber. This is therefore the area which is typically intensively instrumented in order to obtain enough information to characterize the injector performance and injector/wall interaction. Also, installing multiple thermocouples close to the throat can become mechanically challenging due to the small distance between the cooling channels.

Moreover, throughout this section, the position of the thermocouples will be referenced as described in Fig. 10. The first thermocouple is at distance d_1 from the wall, whereas the position of the second thermocouple is given by the relative distance δ with respect to the first sensor. The third thermocouple is located at a distance d_3 from the hot-gas wall. To generalize the results, all distances are given relative to the wall thickness t.

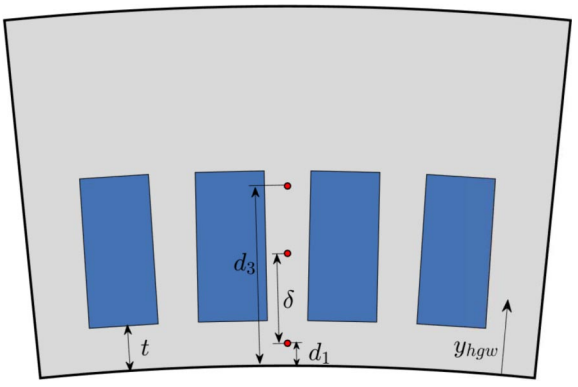

Fig. 10 Overview of the thermocouple positions.

To provide a sufficient axial resolution, 30 thermocouple positions are chosen, with a relative distance of approximately 40 mm from each other. Note that for all analyses the error due to the positioning of the thermocouples, the accuracy of the sensors, and the axial spacing are neglected, as they affect all different methods similarly. Their effect has been discussed in previous studies [4]. For that reason, although the experimental measurements in this Paper are replaced by conjugate heat transfer CFD results, no random error is added to the thermocouple readings. The effect of random measurement noise $\Delta \boldsymbol{T}_{\mathrm{noise}}$ on the obtained inverse heat flux results has been analyzed in previous studies and scales as $\Delta \boldsymbol{Q} = \boldsymbol{S}^{-1} \cdot \Delta \boldsymbol{T}_{\mathrm{noise}}$ [20] and has the same effect on all inverse methods presented in this section. In this context, $\boldsymbol{S}$ is the sensitivity matrix introduced in Eq. (13).

A metric used for comparison of each method's performance is the average heat flux and hot-gas wall temperature error. Those are defined as the average systematic error for all K axial positions as elaborated in Eqs. (7) and (8):

$$\dot{q}_{\mathrm{err}}(d_1, \delta) = \frac{1}{K} \sum_{k=1}^{K} \frac{|\dot{q}_{\mathrm{exact}} - \dot{q}_{\mathrm{calc}}(d_1, \delta)|}{\dot{q}_{\mathrm{exact}}} \tag{7}$$

$$T_{\mathrm{err}}(d_1, \delta) = \frac{1}{K} \sum_{k=1}^{K} \frac{|T_{\mathrm{exact}} - T_{\mathrm{calc}}(d_1, \delta)|}{T_{\mathrm{exact}}} \tag{8}$$

A. Gradient Method

The gradient method is the computationally least expensive one and is shown here as a reference, as it has been applied in various studies in the past. In the presence of cooling channels, the validity of Eq. (2) deteriorates, and an error is expected both for the calculated heat flux and the wall temperature.

The dependence of the magnitude of the resulting errors as a function of the thermocouple positions is plotted in Fig. 11. Note that the upper right corner corresponds to combinations that are not in the liner domain and are hence unfeasible.

Starting with the heat flux error, a rather complex behavior is observed, with high gradients in the resulting error, inferring a large sensitivity on the location of the sensors. For small values of d_1 and δ, the deviation is smaller than 10% (white isoline), but only in a very limited region. Increasing the radial distance of either sensor leads to a rapid increase in the error of the measured heat flux, with the highest deviation reaching up to 85%. A further increase of the sensor position d_1 seems to counterintuitively improve the situation, leading to the existence of a narrow band where $\dot{q}_{\mathrm{err}} \leq 10\%$. This region is, however, the location where the error in heat flux changes sign, going from an overestimation of the heat loads to an underestimation and cannot be predicted a priori. Because no predictions about this region can be made, there cannot be a systematic positioning of the sensors within this region.

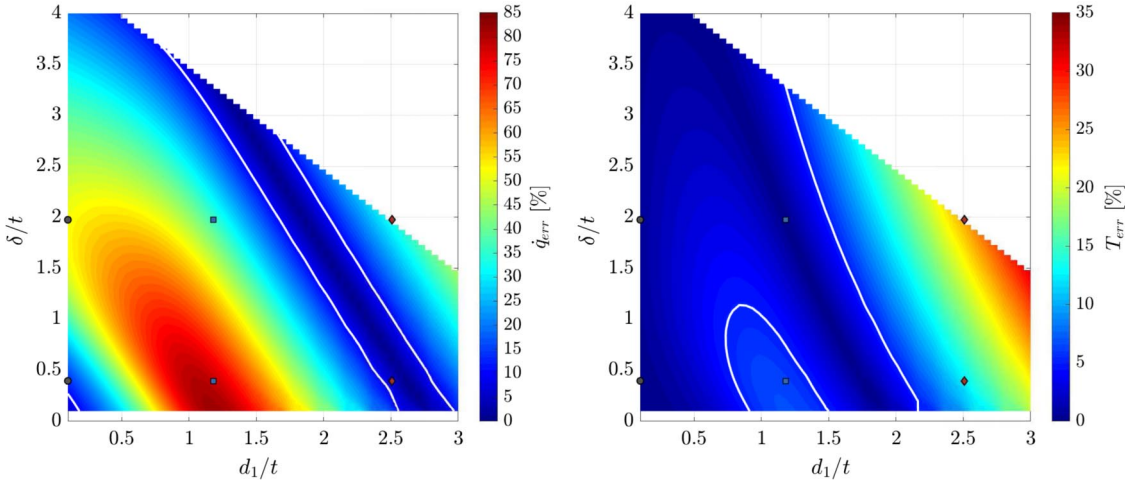

Fig. 11 Heat flux (left) and hot gas wall temperature (right) error for the gradient method. The white isoline corresponds to 10 and 5% error, respectively.

Moreover, looking at the temperature error in the right subfigure, it becomes clear that, even if the heat flux accidentally matches the exact values in this region, the temperature error is not negligible, as it lies outside the region with $T_{\text{err}} \leq 5\%$. It has to be mentioned that the dependence of T_{err} on the thermocouple positions seems to be less sensitive than for the heat flux. Although a larger error is to be expected for larger d_1 values, the gradients remain small, and a large region can be found where the $T_{\text{err}} \leq 5\%$ constraint is met.

It is evident, however, that in order to minimize both the heat flux and hot-gas wall temperature simultaneously the options for the sensor placement are hugely restricted to positions in the imminent vicinity of the wall. Because this is often not feasible from a manufacturing point of view (long thin thermocouple holes combined with a small wall thickness), errors larger than 10% in heat flux are usually the norm.

To better understand the error source of the method, the axial heat flux profiles and structural temperatures for six representative sensor combinations are shown in Fig. 12. The combinations correspond to the marker locations in Fig. 11. Focusing on the temperature profiles in the right subfigure, it is obvious that the simplified logarithmic profile of the gradient method cannot capture the dynamics of the cooling channels which lead to a significant distortion of the exact temperature profile.

B. Inverse Method with Nusselt Number Correlation

As explained in Sec. II, one of the options for modeling the heat transfer coefficient in the cooling channels is the use of a simplified one-dimensional Nusselt number correlations. For the present analysis, the correlation proposed by Kraussold [54] has been used due to its previous applications in rocket engine simulations [4,55]. The heat transfer coefficient is then modeled as a function of the Reynolds Re and Prandtl Pr numbers, as well as the channel hydraulic diameter D_h and coolant thermal conductivity λ_f according to Eq. (9):

$$Nu = \frac{h_{\text{cc}} \cdot D_h}{\lambda_f} = 0.024 \cdot Re^{0.8} \cdot Pr^{0.37} \tag{9}$$

It is then applied to the channel boundary as a von Neumann boundary condition along the normal direction $\boldsymbol{n}$:

$$h_{\text{cc}}(T_f - T_w) = \lambda \frac{\partial T}{\partial \boldsymbol{n}}\bigg|_S \tag{10}$$

For the average (bulk) coolant temperature $T_f(x)$, the heat pickup based on the calculated wall heat flux $\dot{q}$ is used,

$$T_f(x) = T_{f,\text{in}} + \int_0^x \frac{2\pi r_{\text{ch}}}{N_{\text{cc}}} \frac{\dot{q}}{\dot{m} c_p} \text{dx} \tag{11}$$

where N_{cc} stands for the number of the cooling channels.

The solution of the direct problem is carried out using the commercial code ANSYS Fluent [43]. An extensive mesh convergence study has been performed for the grid of the chamber's structure, and

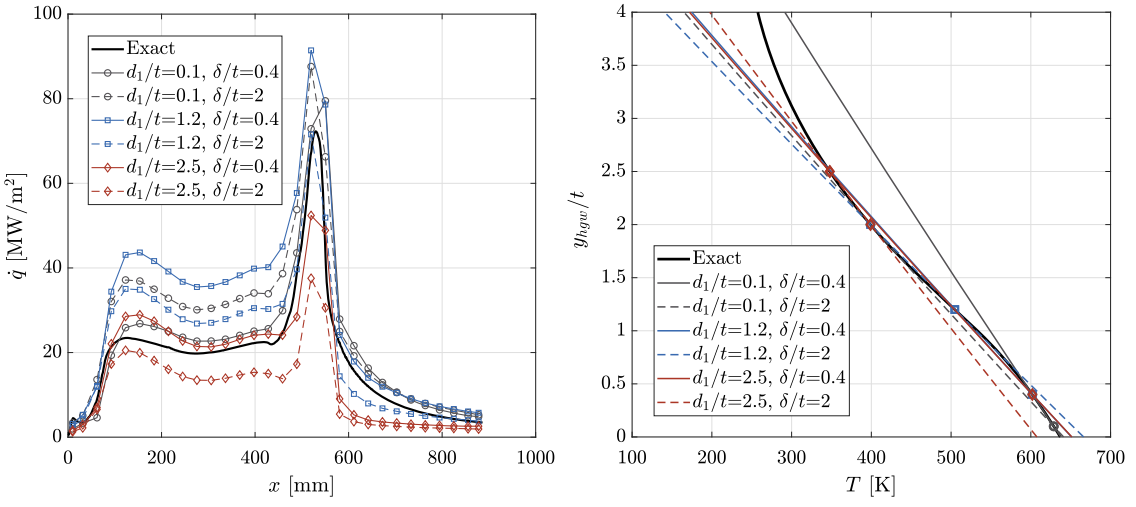

Fig. 12 Axial heat flux profiles for the gradient method (left) and liner temperature profiles for $x = 300$ mm (right).

it was found that the temperature error resulting from the solution of the energy equation in the numerical domain is two orders of magnitude smaller than the sesnors' statistical measurement uncertainty. For that reason, the effect of the computational grid on the retrieved heat flux is not analyzed further.

The calculation of the unknowns, namely, the heat flux at the boundary, is based on a linearization of the problem and follows the Newton–Raphson formulation for the solution of nonlinear systems [56]. The heat flux at each iteration step k is obtained by solving the algebraic equation

$$\boldsymbol{S}\cdot\boldsymbol{Q}^{k+1} = [\boldsymbol{T}_m - \boldsymbol{T}_c(\boldsymbol{Q}^k)] + \boldsymbol{S}\cdot\boldsymbol{Q}^k \tag{12}$$

Solving the system of equations defined in Eq. (12) is carried out using the inversion of the pseudoinverse Moore–Penrose matrix [57], because in the generalized case the problem can be overdetermined (meaning $M \geq N$). It is important to note that the inversion of Eq. (12) is applied on all optimization points simultaneously. Applying the inversion on a reduced set of optimization points (e.g., separately for each axial plane) would lead to a slower convergence due to the neglect of cross-correlation effects.

As shown in previous studies, the Jacobi matrix $\boldsymbol{S}$, which serves as a sensitivity matrix describing the change of the temperature at a thermocouple position due to a small change at a specific heat flux parameter value, can be computed outside of the optimization loop in a preprocessing step [4,20]. This dramatically improves the convergence speed of the algorithm. Its structure is presented in Eq. (13):

$$\boldsymbol{S} = \frac{\partial \boldsymbol{T}}{\partial \boldsymbol{Q}} = \begin{bmatrix} \frac{\partial T_1}{\partial Q_1} & \cdots & \frac{\partial T_M}{\partial Q_1} \\ \vdots & \ddots & \vdots \\ \frac{\partial T_1}{\partial Q_N} & \cdots & \frac{\partial T_M}{\partial Q_N} \end{bmatrix} \tag{13}$$

One of the major benefits of using this method is the need for only one thermocouple for each axial location, as there is only one free parameter to calculate. For that reason, in the analysis shown here, the radial position d_1 is varied, and the resulting heat flux profiles are shown in Fig. 13.

A large discrepancy between the exact and the inverse heat flux profiles can be observed for the largest part of the combustion chamber and up until the throat. The inverse method appears to overestimate the heat flux in the cylindrical part, even for low values of d_1. In general, an increase in the radial distance of the sensor from the wall leads to a lower sensitivity of the method and hence an even further degradation of the agreement with the exact heat flux. This can be supported by the right subfigure of Fig. 13, in which the average temperature and heat flux errors are shown with the black lines and a clear monotonic behavior can be found. Specifically, the average heat flux deviation in the thrust chamber exceeds 40%, whereas the wall temperature prediction is within 5% only for sensor locations very close to the wall ($d_1/t \leq 0.5$).

The smallest chosen value for d_1/t lies at 0.33 (0.5 mm absolute distance in the cylindrical part) and corresponds to an average heat flux error of 40%. It can be observed, however, that the heat flux profile close to the injection plane (first 100 mm) and within the divergent part of the nozzle ($x \leq 600$ mm) matches the exact values with great accuracy, independent of the d_1 value. The reason for the better performance in those locations is the lower stratification of the coolant temperature, as seen when comparing with Fig. 8. Larger stratification caused by large aspect ratios introduces a greater uncertainty in the simplified Nusselt equation, rendering its applicability critical.

The corresponding temperature profiles along the radial direction within the copper liner can be found in Fig. 14. It is evident that the inverse temperature profile is matching the exact one only at the measurement location but shows very large discrepancies for all remaining positions. Increasing the number of thermocouples does not provide any improvement to the solution as the right subfigure of Fig. 14 indicates. Because the form of the temperature profile is strongly influenced by the chosen Nusselt number correlation, the introduction of additional sensors is not sufficient to alter the obtained temperature profile. Instead, for each combination of d_1 and δ, one of the measurements is overestimated, and one of them is underestimated, leading to the local minimum of the optimization algorithm.

Hence, it can be inferred that in the absence of correction functions the use of simplified Nusselt number correlations is not suitable for compressible, supercritical channels flows with high aspect ratio. For that reason, the performance of a correlation, explicitly tailored for supercritical hydrogen cooling channels with high aspect ratios, is assessed. The correlation proposed by Haemisch et al. [58] was derived by examining cooling channels with aspect ratios between 1.7 and 30 and pressure levels up to 160 bar. For hydrogen, the correlation reads

$$Nu = \frac{h_{cc}\cdot D_h}{\lambda_f} = C\cdot Re^{0.8}\cdot Pr^{0.4} \tag{14}$$

where the factor C includes the dependence on the aspect ratio AR:

$$C = 0.005545\cdot e^{-0.2015\cdot \mathrm{AR}} + 0.005207 \tag{15}$$

Applying this correlation to the framework of the inverse method delivers a significant improvement of the heat flux results, which

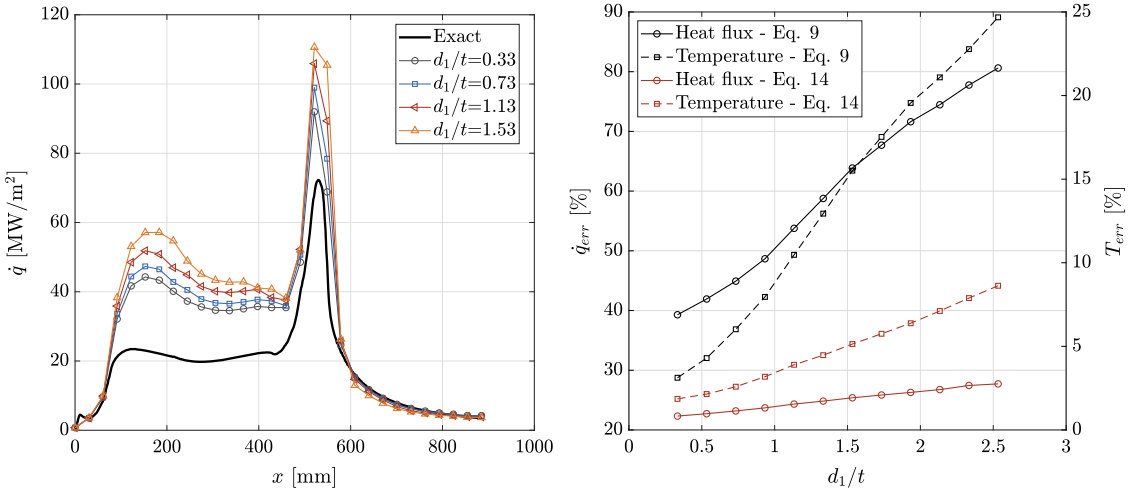

Fig. 13 Axial heat flux profiles (left) and average measurement error (right) for the inverse method using the Kraussold correlation [54] and a single thermocouple.

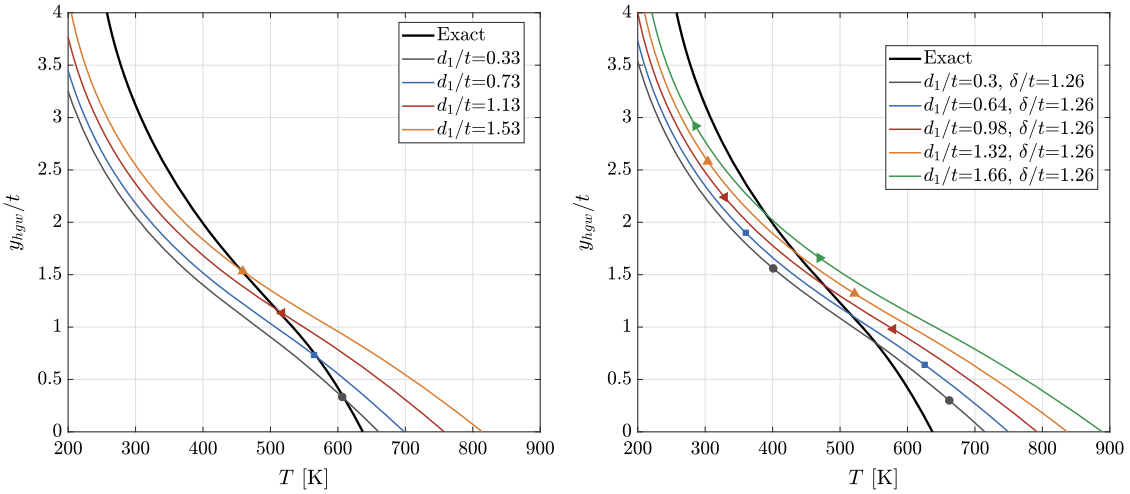

Fig. 14 Liner temperature profiles for $x = 300$ mm using one sensor (left) and two sensors (right) with the Kraussold [54] correlation.

are plotted in Fig. 15. The deviation of the inverse profile remains within 10–15% in the cylindrical part of the chamber and only shows larger discrepancies in the vicinity of the throat. This is expected as the correlation was derived for straight cooling channels and has not been adapted for curvature effects. Still, the average heat flux and wall temperature errors shown in the right subfigure of Fig. 13 in red are in an acceptable range, given the simplicity of the method. Similar to the use of the Kraussold correlation, an increase in d_1 leads to a less accurate prediction, but the sensitivity of the exact thermocouple placement is lower, as the flatter curves indicate.

C. Inverse Method with Simultaneous $\dot{q} - h$ Estimation

It is obvious that using a Nusselt number correlation for the estimation of the heat flux needs to be accompanied by a small uncertainty of the chosen equation and certainty that it captures all the fuel-specific and geometry-specific physical effects. To alleviate the need for fulfillment of those requirements, the heat transfer coefficient can be treated as an unknown optimization parameter of the inverse method and be estimated simultaneously to the heat flux. This way, the cooling channel is treated like a black box, and the need for modeling is kept at a minimum.

This method has been employed in the past to evaluate experimental data [59]. However, because of the large number of unknowns, the inverse algorithm can easily become computationally slow, and an efficient optimization method is required for three-dimensional problems. Taking advantage of the linearity of the problem, the Jacobi-based inversing algorithm from Eq. (12) can be extended to account for the heat transfer coefficient parameter set $\boldsymbol{H}$.

Using the Newton–Raphson method, the update of the unknown parameters is carried out using Eq. (16),

$$\left[c_1 \cdot \frac{\partial \boldsymbol{T}}{\partial \boldsymbol{Q}}, c_2 \cdot \frac{\partial \boldsymbol{T}}{\partial \boldsymbol{H}}\right] \cdot \begin{bmatrix} \boldsymbol{Q}^{k+1} \\ \boldsymbol{H}^{k+1} \end{bmatrix} = [\boldsymbol{T}_m - \boldsymbol{T}_c(\boldsymbol{Q}^k, \boldsymbol{H}^k)] + \left[c_1 \cdot \frac{\partial \boldsymbol{T}}{\partial \boldsymbol{Q}}, c_2 \cdot \frac{\partial \boldsymbol{T}}{\partial \boldsymbol{H}}\right] \cdot \begin{bmatrix} \boldsymbol{Q}^{k} \\ \boldsymbol{H}^{k} \end{bmatrix} \tag{16}$$

where the c_1 and c_2 prefactors ensure that the Jacobians of $\boldsymbol{Q}$ and $\boldsymbol{H}$ have similar orders of magnitude to avoid close-to-singular matrices. For the method to be computationally efficient, the calculation of the sensitivity matrix $\partial \boldsymbol{T}/\partial \boldsymbol{H}$ has to be carried out in a preprocessing step, outside the main optimization loop. This is done by means of a forward finite difference method,

$$\frac{\partial \boldsymbol{T}}{\partial H_i} = \frac{\boldsymbol{T}_c(\boldsymbol{Q}^0, \boldsymbol{H}^0 + \epsilon \cdot \boldsymbol{H}_i^0) - \boldsymbol{T}_c(\boldsymbol{Q}^0, \boldsymbol{H}^0)}{\epsilon \cdot \boldsymbol{H}_i^0} \tag{17}$$

with ϵ being a number small enough for the first-order approximation of the finite difference to be valid. $\boldsymbol{H}_i^0$ is a vector, and its elements $H_{i,j}^0$ are defined as

$$H_{i,j}^0 = \begin{cases} 0 & i \neq j \\ H_i^0 & i = j \end{cases} \tag{18}$$

The choice of the initial guess for the heat flux $\boldsymbol{Q}^0$ and $\boldsymbol{H}^0$ has to be close to the expected results in order to ensure that the linearity of the problem is preserved. For the current analysis, the empirical profiles from Bartz [2] and Haemisch et al. [58] are used for $\boldsymbol{Q}^0$ and $\boldsymbol{H}^0$, respectively. With this newly proposed optimization method, the convergence of the three-dimensional problem with 30 optimization positions (60 free parameters in total) has been found to converge to residuals as low as $J = 0.1$ K^2 within 10–20 iterations, amounting to 2–4 processor hours (CPUh) in total on a workstation with Intel Core i7-6700 3.4 GHz using four cores.

Using this method, two separate studies are carried out, in which the location of the thermocouples are varied. In the first study, two thermocouples are used with varying d_1 and δ, whereas in the second one, a third sensor at a constant position $d_3/t = 4$ is added.

In the first case, using two thermocouples leads to the error distribution shown in Fig. 16. A large region where the heat flux and wall temperature deviations do not exceed 10 and 5%, respectively, can be

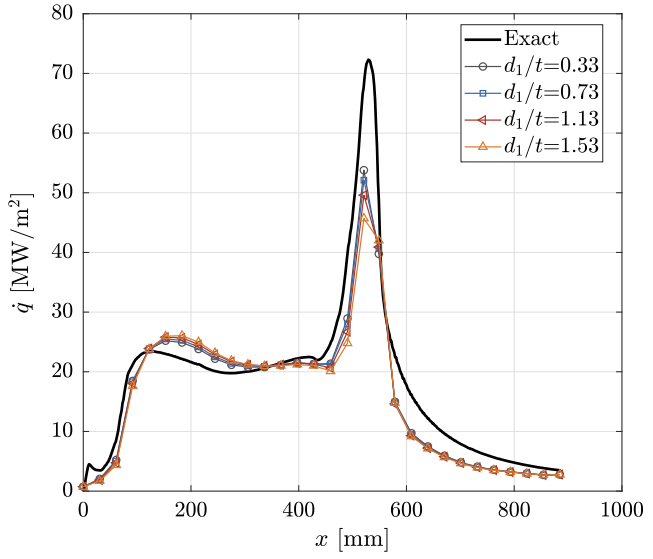

Fig. 15 Axial heat flux profiles for the inverse method using the Haemisch et al. correlation [58] and a single thermocouple.

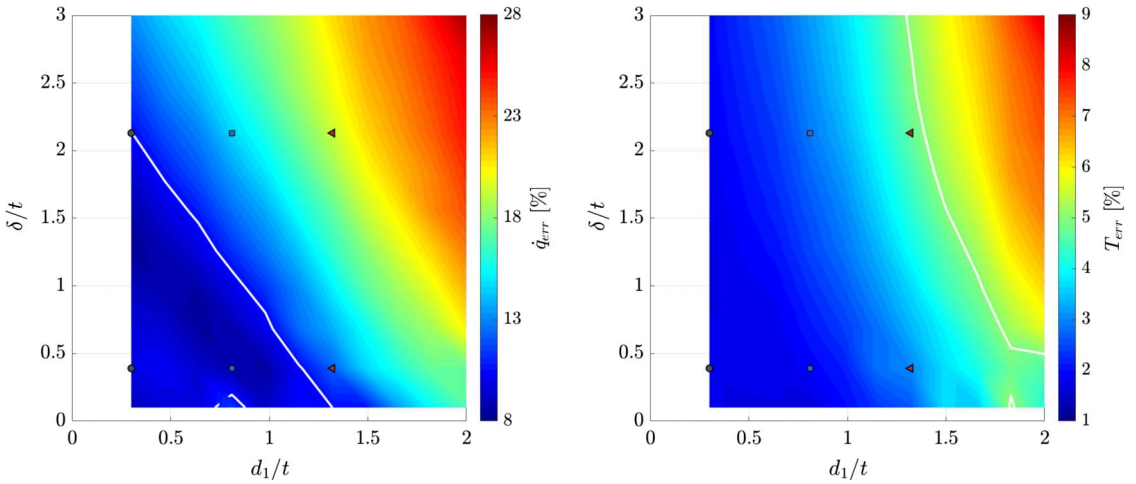

Fig. 16 Heat flux (left) and hot gas wall temperature (right) error for the $\dot{q} - h$ method using two thermocouples. The white isoline corresponds to 10 and 5% error, respectively.

identified. This implies that the positioning of the thermocouples is not as strict as in the case of the Nusselt number correlations. The expected trend seen already in Sec. IV.B is reproduced, with higher values for d_1 leading to an increase in the measurement error.

The axial evolution of the heat flux profiles for selected $d_1 - \delta$ combinations is shown in the diagram of Fig. 17. It can be observed that the exact heat flux profile is reproduced accurately for the entirety of the chamber length. At the same time, the prediction of the average cooling channel heat transfer coefficient can now be compared to the exact profile from the virtual experiment as displayed in the right subfigure of Fig. 17. It has to be noted that the h profiles are not expected to match the exact values perfectly, as the real profiles exhibit a strong variability as shown in Fig. 9 and the assumption of homogeneous h_{cc} coefficient is an oversimplification.

Nevertheless, the obtained curves are demonstrating a qualitative agreement with the exact values. They capture both the initial large values due to the buildup of the boundary layer, the increase in the throat, and the subsequent drop in the divergent nozzle part. Contrary to the heat flux estimation, however, where thermocouples closer to the wall delivered a superior accuracy, in the case of the cooling channels, larger values of d_1 and δ give rise to a better agreement. This is understandable because higher radial positions capture a larger domain of influence of the coolant flow.

To balance out the tradeoff between wall heat flux and cooling channel coefficient accuracy, a further thermocouple is introduced to the system, at the position $d_3/t = 4$. An improvement is observed in the prediction of the heat transfer coefficient in Fig. 18, while the heat flux prediction is not influenced significantly. The improved predictive accuracy of the method is also reflected in the temperature profiles shown in Fig. 19. Including an additional measurement point at $d_3/t = 4$ provides a better matching of the temperature profile, especially for larger radial distances, without significantly changing the hot-gas wall temperature.

D. Inverse Method with Simultaneous $\dot{q} - h_{\text{top}} - h_{\text{bottom}}$ Estimation

A very satisfying agreement with regard to heat flux and wall temperature is achieved using the simultaneous $\dot{q} - h$ optimization while employing two and three sensors. However, because a single value is obtained for the average heat transfer coefficient, little information can be inferred regarding the degree of stratification and the nature of the secondary flows in the channel. If the goal of the experiment and thermocouple measurements is to evaluate the conditions within the cooling channels apart from only the hot-gas heat flux and wall temperature, then the parameterization of the cooling channel using more than one unknowns is recommended.

To demonstrate this effect, the cooling channels are discretized in three separate boundaries: the top, side, and bottom walls. To simplify the problem and based on the expected results from Fig. 9, only the coefficient on the top and bottom boundaries is calculated, and a linear profile is used on the side wall. The linear profile is defined as

$$h_{\text{side}}(y_n) = h_{\text{bottom}} + (h_{\text{top}} - h_{\text{bottom}}) \cdot y_n \tag{19}$$

This discretization method has been applied in the past but with a reduced number of free parameters due to the linear profile assumed for the wall heat load [19].

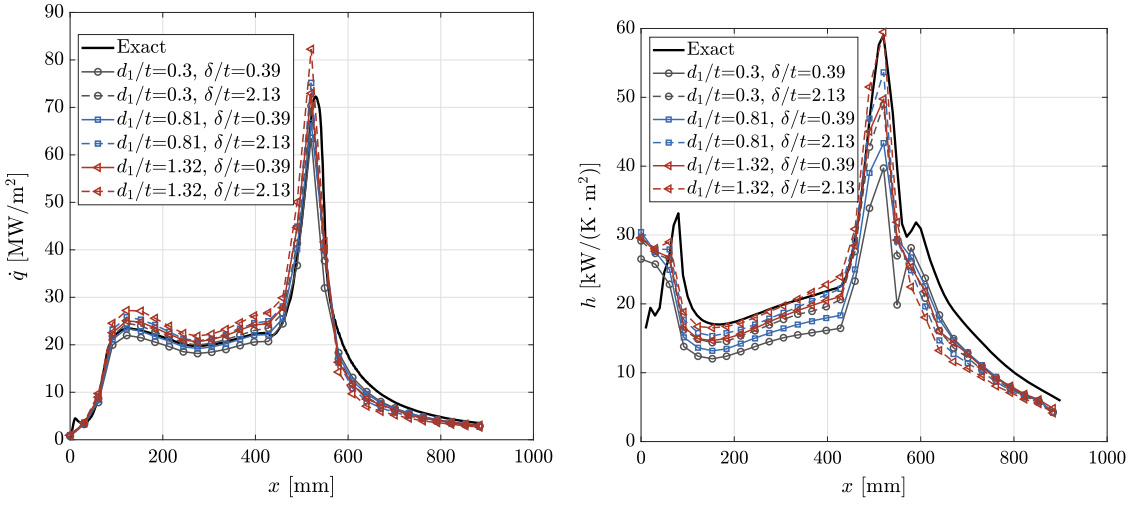

Fig. 17 Axial heat flux profiles (left) and cooling channel heat transfer coefficient profiles (right) for the $\dot{q} - h$ optimization with two sensors.

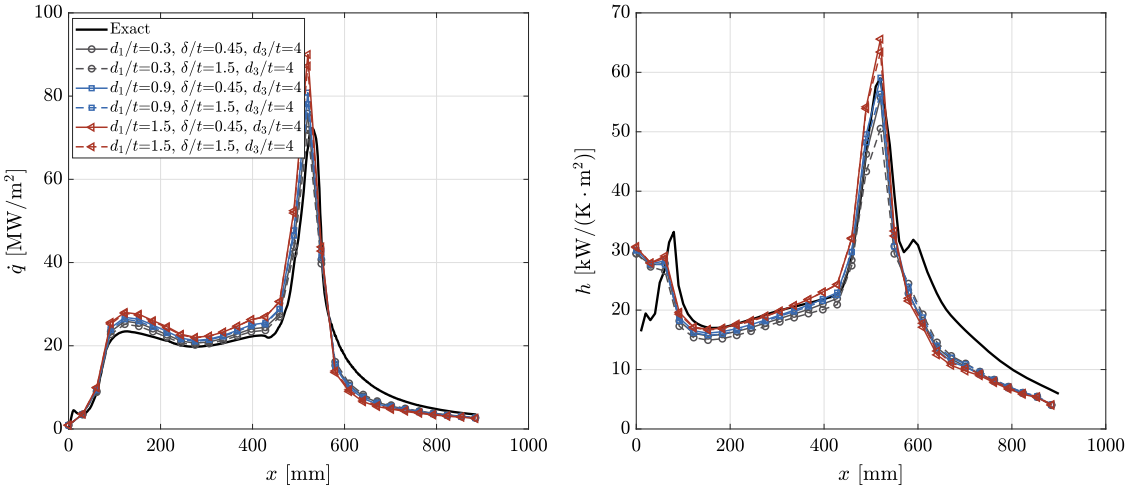

Fig. 18 Axial heat flux profiles (left) and cooling channel heat transfer coefficient profiles (right) for the $\dot{q} - h$ optimization with three sensors. The left and right subfigures share the same legend.

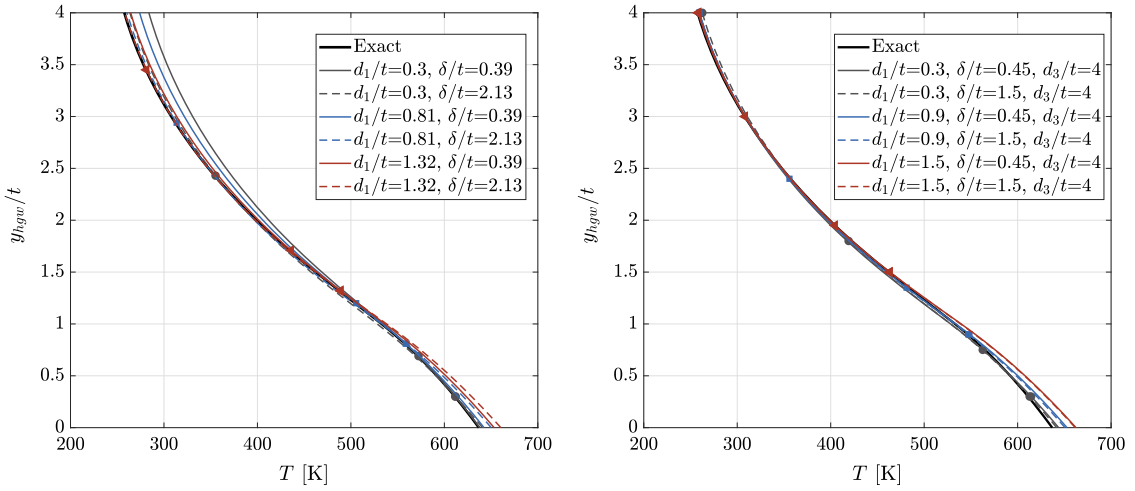

Fig. 19 Liner temperature profiles for the $\dot{q} - h$ optimization using two sensors (left) and three sensors (right) at $x = 300$ mm.

In the present Paper, the optimization method introduced in Eq. (16) is extended to three variables for $\boldsymbol{Q}$, $\boldsymbol{H}_{\text{top}}$, and $\boldsymbol{H}_{\text{bottom}}$. However, because of the introduction of the new variable and the assumed profile of the side wall, the assumption of constant Jacobian is no longer as robust as with two variables. For that reason, first a $\dot{q} - h$ optimization is carried out as a precursor run. Given the converged values for $\boldsymbol{Q}$ and $\boldsymbol{H}$, a new Jacobian is calculated, which can be used for the $\dot{q} - h_{\text{top}} - h_{\text{bottom}}$ run, thereby accelerating the optimization algorithm. Per run, a total of 40–70 iterations was needed, amounting to 8–15 CPUh in total on a workstation with Intel Core i7-6700 at 3.4 GHz using four cores.

The results for the bottom and top walls are shown in Fig. 20. Both profiles appear to be captured by the inverse method throughout the entirety of the domain, with the exception of the throat, where larger

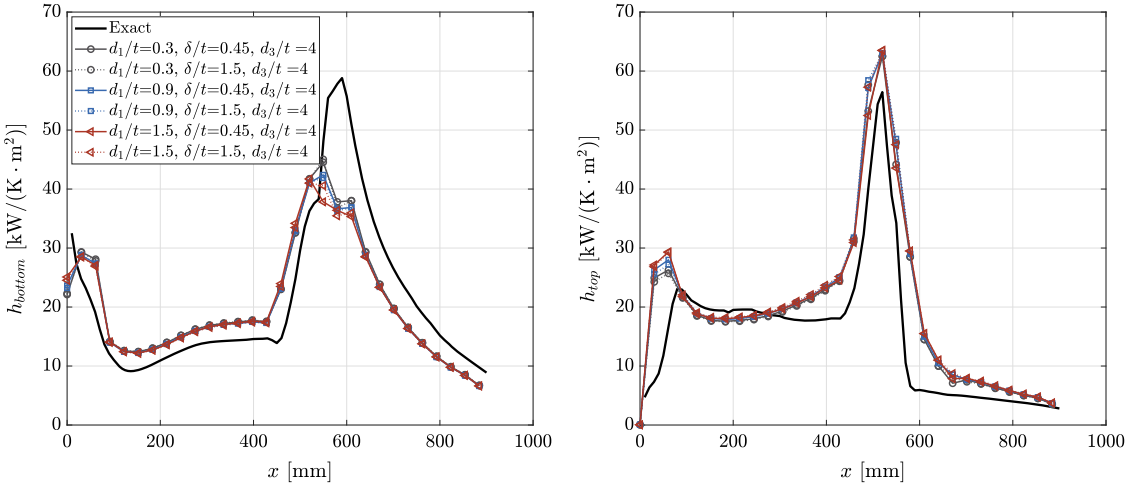

Fig. 20 Cooling channel heat transfer coefficient for the bottom and top walls. The left and right subfigures share the same legend.

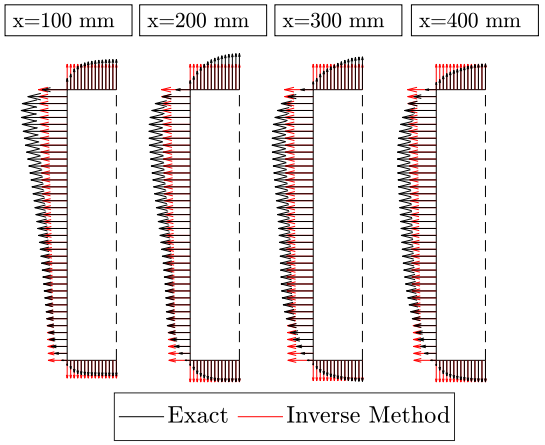

Fig. 21 Heat transfer coefficient along the channel circumference for different axial positions.

deviations are observed. Moreover, the exact positions of the thermocouples do not influence the obtained results significantly, which is encouraging regarding the placement of the sensors. The relative magnitude of the two wall coefficients is also reproduced accurately: in the cylindrical part, the upper wall has a higher average heat transfer coefficient, whereas in the divergent part of the nozzle, the reverse situation holds.

This is also illustrated schematically in Fig. 21, in which the heat transfer coefficient along the entire circumference is plotted in form of a vector field. Again, it is evident that the exact profile is much more complex than the linear trend assumed for the side wall. Increasing the complexity of the presumed profile would be possible but would necessitate additional thermocouples.

V. Conclusions

In the present Paper, the different options for the evaluation of experimental heat flux profiles in subscale and full-scale engines have been assessed for their performance. Obtaining accurate results for the heat flux using the smallest amount of thermocouples is crucial for the design of the testing hardware, as it can simplify cost- and time-intensive manufacturing steps needed for the placement of the sensors.

For the performed analysis, a full-scale upper-stage expander engine operated with LOX/LH_2 has been chosen. To generate the reference experimental heat flux and temperature fields, a CFD coupled simulation of the hot gas flow, structure, and cooling channels has been carried out. The obtained profiles from CFD represent the exact experimental values, and the different inverse methods have been assessed in their ability to match those values.

The results of the gradient method have been included because of the simplicity of the method. Because of the simplification of neglecting the effect of cooling channels, the possible thermocouple locations which allow for an accurate wall temperature and heat flux calculation are very restricted. Hence, the method is considered to be obsolete when dealing with regenerative cooling.

A major improvement can be achieved with the use of inverse methods and the modeling of the cooling channel heat transfer with an algebraic Nusselt number model. The benefit of this method is the large computational speed and the need for only one temperature sensor per axial location, which leads to the smallest possible installation of thermocouples. However, the studies carried out in this Paper display the need for well-validated Nusselt number correlations, which capture the physical phenomena of the fuel-specific properties, the thruster geometry, and the thermodynamic conditions. With increased CFD and experimental studies dealing with the improvement of those correlations and the use of data-based approaches, the method's robustness and range of application are expected to significantly increase.

Finally, to avoid the need for modeling of the cooling channels, the simultaneous optimization of both the wall heat flux and cooling coefficient has been presented. A Jacobi-based approach has been introduced, which significantly accelerates the convergence of the algorithm. This method requires at least two sensors per axial position but delivers heat flux data and cooling channel heat transfer coefficients with an accuracy of 5–12%. Because of the high accuracy of the method, the installation of the thermocouples does not have to be too close at the hot-gas wall, which can reduce the manufacturing costs and increase the liner wall thickness at the measurement locations. With this method, predicting the heat transfer in each one of the three channel walls (top, bottom, and side) has also been demonstrated, at the expense of installing three sensors per axial position.

For all methods presented in this Paper, the systematic error resulting from the placement of the temperature sensors has been analyzed allowing for a better quantification of the expected heat flux experimental uncertainties in future tests. This, combined with the computational efficiency of the proposed Jacobi-based optimization, allows for an increase in reliability and reduction of numerical cost for the evaluation of three-dimensional full-scale rocket test data.

Acknowledgments

Financial support has been provided by the German Research Foundation in the framework of the Sonderforschungsbereich Transregio 40. The authors gratefully acknowledge the Gauss Centre for Supercomputing e.V. (https://www.gauss-centre.eu) for funding this project by providing computing time on the GCS Supercomputer SuperMUC at Leibniz Supercomputing Centre (https://www.lrz.de/). The authors also thank Christof Roth and Maximilian Mörtl for their contribution to the preliminary computational fluid dynamics studies.

References

[1] Sutton, G. P., *History of Liquid Propellant Rocket Engines*, AIAA, Reston, VA, 2006, Chap. 3. https://doi.org/10.2514/4.868870

[2] Bartz, D. R., "A Simple Equation for Rapid Estimation of Rocket Nozzle Convective Heat Transfer Coefficients," *Jet Propulsion*, Vol. 27, No. 1, 1957, pp. 49–51. https://doi.org/10.2514/8.12572

[3] Chemnitz, A., Sattelmayer, T., Roth, C., Haidn, O., Daimon, Y., Keller, R., Gerlinger, P., Zips, J., and Pfitzner, M., "Numerical Investigation of Reacting Flow in a Methane Rocket Combustor: Turbulence Modeling," *Journal of Propulsion and Power*, Vol. 34, No. 4, 2018, pp. 864–877. https://doi.org/10.2514/1.B36565

[4] Perakis, N., Strauß, J., and Haidn, O. J., "Heat Flux Evaluation in a Multi-Element CH4/O2 Rocket Combustor Using an Inverse Heat Transfer Method," *International Journal of Heat and Mass Transfer*, Vol. 142, Oct. 2019, Paper 118425. https://doi.org/10.1016/j.ijheatmasstransfer.2019.07.075

[5] Suslov, D., Betti, B., Aichner, T., Soller, S., Nasuti, F., and Haidn, O., "Experimental Investigation and CFD-Simulation of the Film Cooling in an O2/CH4 Subscale Combustion Chamber," *Space Propulsion Conference*, Association Aéronautique et Astronautique de France, Paris, France, 2012.

[6] Celano, M. P., Silvestri, S., Bauer, C., Perakis, N., Schlieben, G., and Haidn, O. J., "Comparison of Single and Multi-Injector GOC/CH4 Combustion Chambers," *52nd AIAA/SAE/ASEE Joint Propulsion Conference*, AIAA Paper 2016-4990, 2016. https://doi.org/10.2514/6.2016-4990

[7] Arnold, R., Suslov, D., and Haidn, O., "Circumferential Film Cooling Effectiveness in a LOX/H2 Subscale Combustion Chamber," *Journal of Propulsion and Power*, Vol. 25, No. 3, 2009, pp. 760–770. https://doi.org/10.2514/1.40305

[8] Deridder, M. A., and Anderson, W. E., "Heat Flux and Pressure Profiles in an Oxygen/Hydrogen Multielement Rocket Combustor," *Journal of Propulsion and Power*, Vol. 26, No. 4, 2010, pp. 696–705. https://doi.org/10.2514/1.48060

[9] Daimon, Y., Negishi, H., Koshi, M., and Suslov, D., "Numerical and Experimental Investigation of the Methane Film Cooling in Subscale Combustion Chamber," *Progress in Propulsion Physics*, Vol. 8, 2016, pp. 129–144. https://doi.org/10.1051/eucass/2016081290

[10] Oschwald, M., Suslov, D., Haemisch, J., Haidn, O., Celano, M., Kirchberger, C., Rackemann, N., Preuß, A., and Wiedmann, D., *Measurement of Heat Transfer in Liquid Rocket Combustors*, AIAA, Reston, VA, 2020, Chap. 7, pp. 281–331. https://doi.org/10.2514/5.9781624105814.0281.0332

[11] Ash, R., and Wright, R., Jr., "Design Considerations for Gardon Heat Flux Sensors," *6th Thermophysics Conference*, AIAA Paper 1971-470, 1971. https://doi.org/10.2514/6.1971-470

[12] Mityakov, A. V., Sapozhnikov, S. Z., Mityakov, V. Y., Snarskii, A. A., Zhenirovsky, M. I., and Pyrhönen, J. J., "Gradient Heat Flux Sensors for High Temperature Environments," *Sensors and Actuators A: Physical*, Vol. 176, April 2012, pp. 1–9. https://doi.org/10.1016/j.sna.2011.12.020

[13] Celano, M., Silvestri, S., Pauw, J., Perakis, N., Schily, F., Suslov, D., and Haidn, O., "Heat Flux Evaluation Methods for a Single Element Heat-Sink Chamber," *6th European Conference of Aeronautics and Space Science*, EUCAS, Saix, France, 2015.

[14] Perakis, N., Rahn, D., Haidn, O. J., and Eiringhaus, D., "Heat Transfer and Combustion Simulation of Seven-Element O2/CH4 Rocket Combustor," *Journal of Propulsion and Power*, Vol. 35, No. 6, 2019, pp. 1080–1097. https://doi.org/10.2514/1.B37402

[15] Ozisik, M. N., *Inverse Heat Transfer: Fundamentals and Applications*, CRC Press, Boca Raton, FL, 2000, Chap. 2.

[16] Fernández-Torrijos, M., Sobrino, C., Almendros-Ibáñez, J., Marugán-Cruz, C., and Santana, D., "Inverse Heat Problem of Determining Unknown Surface Heat Flux in a Molten Salt Loop," *International Journal of Heat and Mass Transfer*, Vol. 139, Aug. 2019, pp. 503–516. https://doi.org/10.1016/j.ijheatmasstransfer.2019.05.002

[17] Zhang, L., Li, L., Ju, H., and Zhu, B., "Inverse Identification of Interfacial Heat Transfer Coefficient Between the Casting and Metal Mold Using Neural Network," *Energy Conversion and Management*, Vol. 51, No. 10, 2010, pp. 1898–1904. https://doi.org/10.1016/j.enconman.2010.02.020

[18] Huang, C.-H., and Lee, C.-T., "An Inverse Problem to Estimate Simultaneously Six Internal Heat Fluxes for a Square Combustion Chamber," *International Journal of Thermal Sciences*, Vol. 88, Feb. 2015, pp. 59–76. https://doi.org/10.1016/j.ijthermalsci.2014.08.021

[19] Haemisch, J., Suslov, D., and Oschwald, M., "Experimental Analysis of Heat Transfer Deterioration and Pseudoboiling Phenomena in a Methane Cooled Combustion Chamber at Real Conditions," *2018 Joint Propulsion Conference*, AIAA Paper 2018-4943, 2018. https://doi.org/10.2514/6.2018-4943

[20] Perakis, N., and Haidn, O. J., "Inverse Heat Transfer Method Applied to Capacitively Cooled Rocket Thrust Chambers," *International Journal of Heat and Mass Transfer*, Vol. 131, March 2019, pp. 150–166. https://doi.org/10.1016/j.ijheatmasstransfer.2018.11.048

[21] Dabrowski, A., and Dabrowski, L., "Inverse Heat Transfer Problem Solution of Sounding Rocket Using Moving Window Optimization," *PLOS One*, Vol. 14, No. 6, 2019, Paper e0218600. https://doi.org/10.1371/journal.pone.0218600

[22] Luo, J., and Shih, A. J., "Inverse Heat Transfer Solution of the Heat Flux due to Induction Heating," *Journal of Manufacturing Science and Engineering*, Vol. 127, No. 3, 2005, pp. 555–563. https://doi.org/10.1115/1.1949617

[23] Huang, C.-H., and Tsai, Y.-L., "A Transient 3-D Inverse Problem in Imaging the Time-Dependent Local Heat Transfer Coefficients for Plate Fin," *Applied Thermal Engineering*, Vol. 25, Nos. 14–15, 2005, pp. 2478–2495. https://doi.org/10.1016/j.applthermaleng.2004.12.003

[24] Wang, T., Sun, B., Xiang, J., and Liu, D., "Wall Heat Flux Measurements in a GO2/GH2 Heat-Sink Combustion Chamber," *Journal of Thermal Science and Technology*, Vol. 13, No. 1, 2018, Paper JTST0016. https://doi.org/10.1299/jtst.2018jtst0016

[25] Singh, S. K., Yadav, M. K., Sonawane, R., Khandekar, S., and Muralidhar, K., "Estimation of Time-Dependent Wall Heat Flux from Single Thermocouple Data," *International Journal of Thermal Sciences*, Vol. 115, May 2017, pp. 1–15. https://doi.org/10.1016/j.ijthermalsci.2017.01.010

[26] Raudenský, M., Woodbury, K. A., Kral, J., and Brezina, T., "Genetic Algorithm in Solution of Inverse Heat Conduction Problems," *Numerical Heat Transfer, Part B Fundamentals*, Vol. 28, No. 3, 1995, pp. 293–306. https://doi.org/10.1080/10407799508928835

[27] Szénási, S., and Felde, I., "Configuring Genetic Algorithm to Solve the Inverse Heat Conduction Problem," *2017 IEEE 15th International Symposium on Applied Machine Intelligence and Informatics (SAMI)*, Inst. of Electrical and Electronics Engineers, Piscataway, NJ, 2017, pp. 387–392. https://doi.org/10.1109/SAMI.2017.7880340

[28] Yu, B., Yao, W., Gao, Q., Zhou, H., and Xu, C., "A Novel Non-Iterative Inverse Method for Estimating Boundary Condition of the Furnace Inner Wall," *International Communications in Heat and Mass Transfer*, Vol. 87, Oct. 2017, pp. 91–97. https://doi.org/10.1016/j.icheatmasstransfer.2017.06.017

[29] Yu, B., Xu, C., Yao, W., and Meng, Z., "Estimation of Boundary Condition on the Furnace Inner Wall Based on Precise Integration BEM Without Iteration," *International Journal of Heat and Mass Transfer*, Vol. 122, July 2018, pp. 823–845. https://doi.org/10.1016/j.ijheatmasstransfer.2018.02.039

[30] Nie, C., and Yu, B., "Inversing Heat Flux Boundary Conditions Based on Precise Integration FEM Without Iteration and Estimation of Thermal Stress in FGMs," *International Journal of Thermal Sciences*, Vol. 140, June 2019, pp. 201–224. https://doi.org/10.1016/j.ijthermalsci.2019.03.003

[31] Fadale, T. D., Nenarokomov, A. V., and Emery, A. F., "Two Approaches to Optimal Sensor Locations," *Journal of Heat Transfer*, Vol. 117, No. 2, 1995, pp. 373–379. https://doi.org/10.1115/1.2822532

[32] Wan, S., Xu, P., Wang, K., and Li, S., "Estimation of Distributed Thermal Boundary Based on Fuzzy Clustering of Temperature Observable Points," *International Journal of Heat and Mass Transfer*, Vol. 147, Feb. 2020, Paper 118920. https://doi.org/10.1016/j.ijheatmasstransfer.2019.118920

[33] Pizzarelli, M., Nasuti, F., Paciorri, R., and Onofri, M., "Numerical Analysis of Three-Dimensional Flow of Supercritical Fluid in Cooling Channels," *AIAA Journal*, Vol. 47, No. 11, 2009, pp. 2534–2543. https://doi.org/10.2514/1.38542

[34] Dang, G., Zhong, F., Zhang, Y., and Zhang, X., "Numerical Study of Heat Transfer Deterioration of Turbulent Supercritical Kerosene Flow in Heated Circular Tube," *International Journal of Heat and Mass Transfer*, Vol. 85, June 2015, pp. 1003–1011. https://doi.org/10.1016/j.ijheatmasstransfer.2015.02.052

[35] Pizzarelli, M., Urbano, A., and Nasuti, F., "Numerical Analysis of Deterioration in Heat Transfer to Near-Critical Rocket Propellants," *Numerical Heat Transfer, Part A: Applications*, Vol. 57, No. 5, 2010, pp. 297–314. https://doi.org/10.1080/10407780903583016

[36] Pizzarelli, M., "A CFD-Derived Correlation for Methane Heat Transfer Deterioration," *Numerical Heat Transfer, Part A: Applications*, Vol. 69, No. 3, 2016, pp. 242–264. https://doi.org/10.1080/10407782.2015.1080575

[37] Pioro, I. L., Khartabil, H. F., and Duffey, R. B., "Heat Transfer to Supercritical Fluids Flowing in Channels–Empirical Correlations (Survey)," *Nuclear Engineering and Design*, Vol. 230, Nos. 1–3, 2004, pp. 69–91. https://doi.org/10.1016/j.nucengdes.2003.10.010

[38] Naraghi, M., and Dassonville, R., "Improved Correlations for Curvature Effects in Cooling Channels of Rocket Engines," *48th AIAA/ASME/SAE/ASEE Joint Propulsion Conference & Exhibit*, AIAA Paper 2012-3992, 2012. https://doi.org/10.2514/6.2012-3992

[39] Waxenegger-Wilfing, G., Dresia, K., Deeken, J. C., and Oschwald, M., "Heat Transfer Prediction for Methane in Regenerative Cooling Channels with Neural Networks," *Journal of Thermophysics and Heat Transfer*, Vol. 34, No. 2, 2020, pp. 347–357. https://doi.org/10.2514/1.T5865

[40] Eiringhaus, D., Riedmann, H., Knab, O., and Haidn, O. J., "Full-Scale Virtual Thrust Chamber Demonstrators as Numerical Testbeds Within SFB-TRR 40," *Joint Propulsion Conference*, AIAA Paper 2018-4469, 2018. https://doi.org/10.2514/6.2018-4469

[41] Haidn, O. J., Adams, N., Radespiel, R., Schröder, W., Stemmer, C., Sattelmayer, T., and Weigand, B., "Fundamental Technologies for the Development of Future Space Transport System Components Under High Thermal and Mechanical Loads," *Joint Propulsion Conference*, AIAA Paper 2018-4466, 2018. https://doi.org/10.2514/6.2018-4466

[42] Santiago, J., "Evolution of the RL10 Liquid Rocket Engine for a New Upperstage Application," *32nd Joint Propulsion Conference and Exhibit*, AIAA Paper 1996-3013, 1996. https://doi.org/10.2514/6.1996-3013

[43] Fluent, A., *Ansys Fluent Theory Guide*, ANSYS, Inc., Canonsburg, PA, 2011.

[44] Traxinger, C., Zips, J., and Pfitzner, M., "Large-Eddy Simulation of a Multi-Element LOx/CH4 Thrust Chamber Demonstrator of a Liquid Rocket Engine," *8th European Conference of Aeronautics and Space Science*, EUCAS, Saix, France, 2019. https://doi.org/10.13009/EUCASS2019-731

[45] Negishi, H., Daimon, Y., and Kawashima, H., "Flowfield and Heat Transfer Characteristics in the LE-X Expander Bleed Cycle Combustion Chamber," *50th AIAA/ASME/SAE/ASEE Joint Propulsion Conference*, AIAA Paper 2014-4010, 2014. https://doi.org/10.2514/6.2014-4010

[46] Peng, D.-Y., and Robinson, D. B., "A New Two-Constant Equation of State," *Industrial and Engineering Chemistry Fundamentals*, Vol. 15, No. 1, 1976, pp. 59–64. https://doi.org/10.1021/i160057a011

[47] Abudour, A. M., Mohammad, S. A., Robinson, R. L., Jr., and Gasem, K. A., "Volume-Translated Peng-Robinson Equation of State for Liquid Densities of Diverse Binary Mixtures," *Fluid Phase Equilibria*, Vol. 349, July 2013, pp. 37–55.
https://doi.org/10.1016/j.fluid.2013.04.002

[48] Launder, B. E., and Spalding, D. B., *Mathematical Models of Turbulence*, Academic Press, London, 1972, pp. 101–108.

[49] Wolfshtein, M., "The Velocity and Temperature Distribution in One-Dimensional Flow with Turbulence Augmentation and Pressure Gradient," *International Journal of Heat and Mass Transfer*, Vol. 12, No. 3, 1969, pp. 301–318.
https://doi.org/10.1016/0017-9310(69)90012-X

[50] Chung, T. H., Ajlan, M., Lee, L. L., and Starling, K. E., "Generalized Multiparameter Correlation for Nonpolar and Polar Fluid Transport Properties," *Industrial and Engineering Chemistry Research*, Vol. 27, No. 4, 1988, pp. 671–679.
https://doi.org/10.1021/ie00076a024

[51] Menter, F. R., "Two-Equation Eddy-Viscosity Turbulence Models for Engineering Applications," *AIAA Journal*, Vol. 32, No. 8, 1994, pp. 1598–1605.
https://doi.org/10.2514/3.12149

[52] Lemmon, E., McLinden, M., Friend, D., Linstrom, P., and Mallard, W., *NIST Chemistry WebBook*, NIST Standard Reference Database Number 69, National Inst. of Standards and Technology, Gaithersburg, MD, 2011.

[53] DiValentin, J., and Naraghi, M., "Effects Cooling Channel Curvature on Coolant Secondary Flow and Heat Transfer," *46th AIAA/ASME/SAE/ASEE Joint Propulsion Conference & Exhibit*, AIAA Paper 2010-6973, 2010.
https://doi.org/10.2514/6.2010-6973

[54] Kraussold, H., "Die Wärmeübertragung an Flüssigkeiten in Rohren bei Turbulenter Strömung," *Forschung auf dem Gebiet des Ingenieurwesens A*, Vol. 4, No. 1, 1933, pp. 39–44.
https://doi.org/10.1007/BF02716945

[55] Kirchberger, C., Wagner, R., Kau, H.-P., Soller, S., Martin, P., Bouchez, M., and Bonzom, C., "Prediction and Analysis of Heat Transfer in Small Rocket Chambers," *46th AIAA Aerospace Sciences Meeting and Exhibit*, AIAA Paper 2008-1260, 2008.
https://doi.org/10.2514/6.2008-1260

[56] Fletcher, R., *Practical Methods of Optimization*, Wiley, Hoboken, NJ, 2013, pp. 44–79.

[57] Strang, G., *Linear Algebra and Its Applications*, Hartcourt Brace Jovanovich College, San Diego, CA, 1988, pp. 211–214.

[58] Haemisch, J., Suslov, D., and Oschwald, M., "Experimental Analysis of Heat Transfer Processes in Cooling Channels of a Subscale Combustion Chamber at Real Thermal Conditions for Cryogenic Hydrogen and Methane," *6th Space Propulsion Conference*, Association Aéronautique et Astronautique de France, Paris, France, 2018.

[59] Kuhl, D., Haidn, O., and Holzer, A., "Computational Solution of the Inverse Heat Conduction Problem of Rocket Combustion Chambers," *35th Joint Propulsion Conference and Exhibit*, AIAA Paper 1999-2913, 1999.
https://doi.org/10.2514/6.1999-2913